From an atomic layer to the bulk: Low-temperature atomistic structure and ferroelectric and electronic properties of SnTe films

Thaneshwor P. Kaloni,[1] Kai Chang,[2,3,4] Brandon J. Miller,[1] Qi-Kun Xue,[3,4] Xi Chen,[3,4] Shuai-Hua Ji,[3,4,5] Stuart S. P. Parkin,[2] and Salvador Barraza-Lopez[1,6,*]

[1]*Department of Physics, University of Arkansas, Fayetteville, Arkansas 72701, USA*
[2]*Max-Planck Institute of Microstructure Physics, Halle 06120, Germany*
[3]*State Key Laboratory of Low-Dimensional Quantum Physics, Department of Physics, Tsinghua University, Beijing 100084, China*
[4]*Collaborative Innovation Center of Quantum Matter, Beijing 100084, China*
[5]*RIKEN Center for Emergent Matter Science, Wako, Saitama 351-0198, Japan*
[6]*Institute of Nanoscale Science and Engineering, University of Arkansas, Fayetteville, Arkansas 72701, USA*

(Received 27 September 2018; revised manuscript received 16 March 2019; published 23 April 2019)

SnTe hosts ferroelectricity that competes with its weak nontrivial band topology: in the high-symmetry rocksalt structure—in which its intrinsic electric dipole is quenched—this material develops metallic surface bands, but in its rhombic ground-state configuration—which hosts a nonzero spontaneous electric dipole—the crystalline symmetry is lowered, and the presence of surface electronic bands is not guaranteed. Here, the type of ferroelectric coupling and the atomistic and electronic structure of SnTe films ranging from 2 to 40 atomic layers (ALs) are examined on freestanding samples, to which atomic layers were gradually added. Four-AL SnTe films are antiferroelectrically coupled, while thicker freestanding SnTe films are ferroelectrically coupled. The electronic band gap reduces its magnitude in going from 2 to 40 ALs, but it does not close due to the rhombic nature of the structure. These results bridge the structure of SnTe films from the monolayer to the bulk.

DOI: 10.1103/PhysRevB.99.134108

I. INTRODUCTION

IV-VI compounds can form bulk rocksalt, orthorhombic, or rhombic ground-state structures depending on their average atomic number [1]: PbS is a textbook example of a rocksalt structure [2] that lacks an electric dipole, SnSe is an orthorhombic layered compound with antiferroelectric coupling (labeled *AB*) among successive layers [3,4], and SnTe develops a ferroelectric coupling (labeled *AA*) on its rhombic phase. Bulk SnTe is a well-studied material that nevertheless continues to provide new physical phenomena. Studies exist of its optical and electronic properties [5–9], which include magnetoresistance [10–13], the influence of temperature on electron transport [14], the evolution of theoretical [15–18] and experimental [19–21] electronic band structure methodologies, the relation of carrier concentration and anomalous resistivity with the rhombic to rocksalt phase transition [22–24], and superconductivity [25,26].

Additionally, experimental studies of structural phase transitions on these *diatomic ferroelectrics* were performed with Mösbauer [27] and Raman spectroscopies [28,29], neutron scattering [30–35], and x-ray photoemission [34,36,37]. Theories that explain such transitions based on lattice dynamics have been developed [38–43] with an emphasis on soft-phonon modes [44,45] and on the corresponding softening of elastic constants [46]. The combination of temperature-dependent thermal [47] and electronic conductivities [14,22–24] makes SnTe a model thermoelectric material [35,48]. The rhombic structure and ferroelectric ordering of SnTe occur at temperatures below 150 K with a lattice constant $a_0 = 6.325$ Å and a rhombic angle $\alpha = 89.895^\circ$ [1,28,32,40,49–51] among lattice vectors.

A twist on recreating the parity anomaly by electronic band inversion of the group-IV-VI material family [52,53] culminated in a rediscovery of SnTe as a topological crystalline insulator later on [54,55]. But having a rhombic symmetry, i.e., a lower symmetry than that of a rocksalt structure, its surface electronic states along the (100) direction must be gapped at low temperature [56]. Nowadays, the *coupling* among the temperature-dependent degrees of freedom discussed in previous paragraphs, electronic band structure [57] and thermoelectricity [58], as well as discoveries of higher-order topology [59] continue to find their way to thick SnTe slabs.

At the same time, interest in ultrathin SnTe originated from theoretical predictions of ferroelectricity in these films [60–66] and their experimental fabrication [67,68]. These SnTe slabs were not created by capping a bulk sample but grown from the bottom up [67–70]. And while common theoretical approaches assume a slab can be obtained by cutting two opposing surfaces of bulk rocksalt [54] or rhombic [56,65,71] bulk samples, the present work aims to explore the structural evolution of a freestanding SnTe slab containing $2n$ atomic layers (ALs) by the successive addition of 2 ALs in the *overall lowest-energy conformation* to the slab containing $2(n-1)$ ALs, with n being a positive integer, thus complementing the experimental results of Ref. [68].

Toward this goal, the following points will be established here: (a) 4-AL SnTe films are antiferroelectrically coupled, while thicker suspended SnTe films turn out to be

*sbarraza@uark.edu

 ©2019 American Physical Society

ferroelectrically coupled. (b) In going from 2 to 40 ALs, the rhombic angle $\Delta\alpha$, defined as $90^\circ - \alpha$, decreases from about 2° down to $\sim 0.11^\circ$, which is close to its experimental magnitude in the bulk. The paper is structured as follows: Technical details are provided in Sec. II, followed by results and discussion in Sec. III and conclusions in Sec. IV.

II. TECHNICAL DETAILS

We performed *ab intio* calculations with the SIESTA code [72] (which employs localized numeric atomic orbitals [73] and norm-conserving Troullier-Martins pseudopotentials [74]) with van der Waals corrections of the Berland-Hyldgaard type [75] (also known as cx-vdW-DF1) as implemented by Román-Pérez and Soler [76] on pseudopotentials whose radii were optimized in house [77]. The real-space grid in which the Poisson equation is solved has a cutoff energy of 300 Ry. A Monkhorst-Pack [78] mesh of $18 \times 18 \times 1$ k points was employed in calculations involving unit cells, and a $3 \times 3 \times 1$ k-point mesh was used for calculations on 11×11 supercells containing vacancies. Standard, double-zeta plus polarization (DZP) basis sets [73] with an energy shift of 0.0022 Ry were used. The vertical vacuum among periodic slabs was set to 60 Å, and dipole corrections were turned on. Structural optimizations were performed with a force tolerance of 10^{-3} eV/Å. Spin-orbit coupling was turned on only after the electronic structure was optimized. Simulated scanning tunneling microscopy (STM) images [79,80] were obtained by adding the electronic densities of individual wave functions in an energy window consistent with experimental energy ranges, and captured 2.5 Å above the SnTe film (see Refs. [81–83]).

In addition, ultrathin SnTe films were grown on 6*H*-SiC(0001) substrates that were sublimated to host epitaxial graphene layers [84] employing substrate preparation and van der Waals molecular beam epitaxy methods described before [67,68]. STM measurements were carried out at 4.7 K on a Unisoku USM1600 system. The Pt-Ir alloy tip was calibrated on the epitaxial silver islands grown on a Si(111) substrate, and dI/dV experiments were conducted with a signal recovery lock-in amplifier with a V_s modulation frequency of 913 Hz. Sample growth and STM studies were performed in the same vacuum system without exposure to air.

III. RESULTS AND DISCUSSION

A. Structure and STM images of ferroelectric 2-AL SnTe films

The rhombic distortion angle $\Delta\alpha$ in Fig. 1(a) is related to the orthorhombic in-plane lattice parameters a_1 and a_2 by [85]:

$$\frac{a_1}{a_2} = \frac{1 + \sin(\Delta\alpha)}{\cos(\Delta\alpha)}. \quad (1)$$

At low temperature and in ultrathin films, SnTe displays values of $\Delta\alpha$ no larger than 3° which, as seen in Fig. 1(b), permits approximating $\Delta\alpha$ as $a_1/a_2 - 1$ (in radians). Experimentally, the 2 AL SnTe film schematically shown in Fig. 1(c) registers a value $\Delta\alpha = 1.4 \pm 0.1^\circ$ at 4 K. In our calculations, $a_1 = 4.728$ Å and $a_2 = 4.567$ Å for $\Delta\alpha = 2.02^\circ$. Figure 1(c) displays a side view of two unit cells of the 2-AL SnTe film in

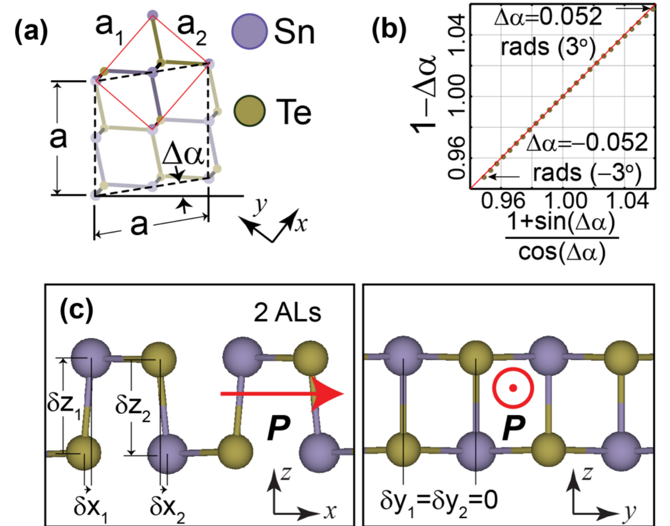

FIG. 1. (a) Definition of the rhombic distortion angle $\Delta\alpha$. (b) Demonstration of the linear relation among $1 + \Delta\alpha$ and $[1 + \sin(\Delta\alpha)]/\cos(\Delta\alpha)$ up to $\pm 3^\circ$. (c) Side views for 2-AL SnTe. Arrows in (c) indicate the spontaneous polarization $\mathbf{P}$, while δx_i, δy_i, and δz_i ($i = 1, 2$) are atomic displacements leading to such spontaneous polarization.

which the direction of the intrinsic electric dipole $\mathbf{P}$ is shown explicitly.

Experimental dI/dV curves (top panels) and simulated density of states (DOS) data (bottom panels) are presented for a 2 AL SnTe film in Fig. 2. The valence band edge on the DOS has been horizontally displaced to match the experimental band edge, so that simulated STM images are integrated down to energies consistent with experiment. The experimental dI/dV curve in Fig. 2(a) shows a peak at the band edge which does not appear on the simulated DOS

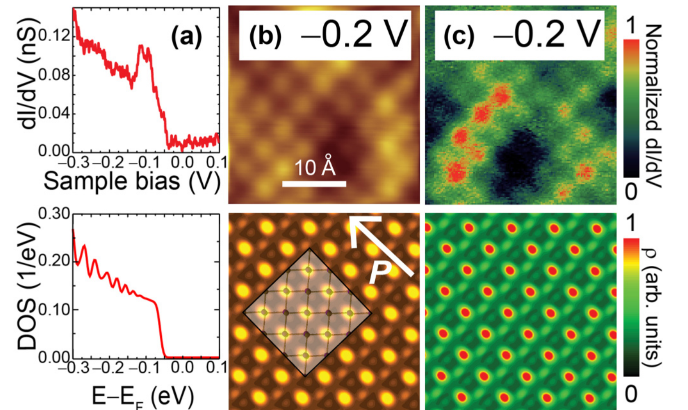

FIG. 2. (a) Experimental dI/dV curve (top) and computed DOS (bottom) for a 2 AL SnTe film. The band edge of the DOS curve is aligned with that of the experimental dI/dV curve in order to integrate the electronic density down to energies consistent with experiment. (b) STM in topographic mode at a bias of -0.2 V (top) and set point current $I_t = 100$ pA and its simulated counterpart (bottom; atomic positions of a 3×3 supercell are overlaid). (c) Top: scanning tunneling spectroscopy images at $V_s = -0.2$ V, with a set point current $I_t = 100$ pA and a sample bias modulation $V_{\rm mod} = 0.001$ V. Bottom: electronic density in between -0.21 and -0.19 eV.

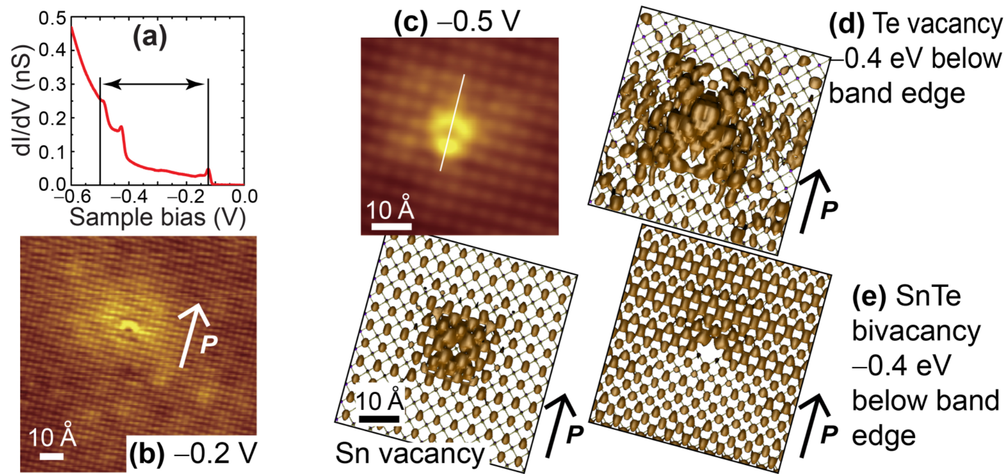

FIG. 3. (a) dI/dV spectrum away from the bright defect seen in subplot (b), which is a topographic STM image of a defect at $V_s = -0.2$ V. (c) Top (bottom): experimental (simulated 3D) topographic image of a defect at -0.5 V. (d) Simulated 3D density image of a Te vacancy. (e) Simulated 3D density image of a SnTe bivacancy. The density in (d) and (e) was integrated down to the leftmost vertical solid line shown in (a) for consistency with the energy range employed in creating subplot (c).

and is likely due to adatoms at the graphene/2 AL SnTe interface, which would be consistent with dark regions on the experimental figure that register a reduced tunneling current. Aside from that abrupt peak at about -0.1 V, the experimental dI/dV and simulated DOS curves can be empirically related by $dI/dV \simeq 0.5 \times$ DOS.

The top plot in Fig. 2(b) is an experimental topographic image in which the energy has been integrated down to -0.2 V, while the bottom plot corresponds to a simulation of the total density from the Fermi energy down to the corresponding experimental energy. Figure 2(c), on the other hand, represents the electronic density within a narrow energy range, i.e., the density created by only a handful of electronic wave functions. The brightest spots that provide the experimental atomic registry in Figs. 2(b) and 2(c), upper subplots, are reproduced in simulations; they correspond to the exposed Sn sublattice, which protrudes farther than the Te atoms according to Fig. 1(c) as emphasized by an overlaid 3×3 atomistic supercell in the lower subplot of Fig. 2(b). The brightest feature in all simulated images looks elongated along the direction parallel to **P**.

B. On the possible type of atomic vacancies

To isolate vacancies and avoid spurious interactions arising from periodic images, a single structural defect (a Sn, Te, or Sn-Te dimer vacancy) was simulated on an 11×11 supercell, making it computationally expensive to observe these defects on films thicker than 2 ALs. Nevertheless, STM images of structural vacancies display high contrast over many atomic sites and have geometrical shapes that ought to be independent of material thickness, giving us confidence that their simulation on a 2 AL SnTe film does provide relevant information representative of exposed vacancies on thicker films.

Figure 3(a) displays the experimental dI/dV profile of a SnTe film with unknown thickness. The direction of the intrinsic electric dipole **P** was obtained from the band bending at crystal edges (not shown) using techniques developed before [67,68]. The bright yellow feature in the STM topography image at $V_s = -0.2$ V and $I_t = 100$ pA in Fig. 3(b) will be shown to surround a Sn vacancy next.

For this purpose, the topographic feature displayed in Fig. 3(a) is shown in the topmost subplot of Fig. 3(c) under a -0.5 V bias with a higher spatial resolution. The bright feature surrounding the dark spot is not radially symmetric, and its axis of symmetry is parallel to the arrow indicating the direction of **P** in Fig. 3(b). The bottom plot of Fig. 3(c) is a simulated three-dimensional (3D) isodensity image for a 2-AL SnTe film on the $3 \times 3 \times 1$ k-point mesh indicated before, rotated to match the orientation of the experimental figure. A spot with no density centered along the Sn vacancy

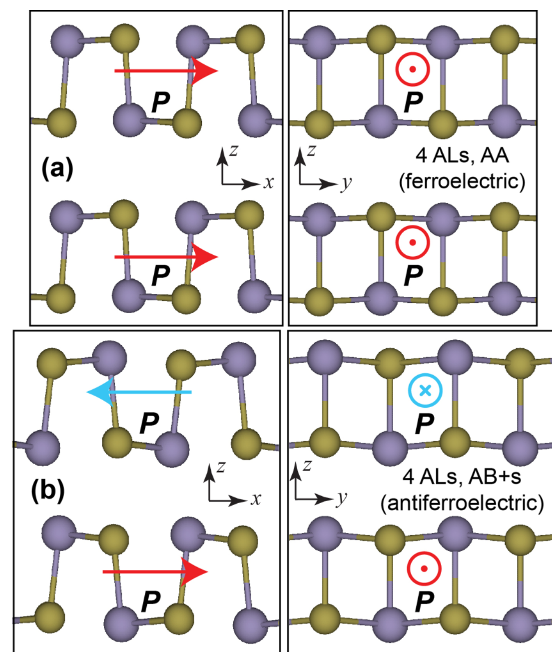

FIG. 4. (a) Four ALs with a ferroelectric (AA) stacking. (b) Four ALs with an antiferroelectric stacking, in which the upper 2 ALs are shifted by $\mathbf{a}_1/2$. Arrows indicate the spontaneous polarization **P** on a given 2 ALs.

TABLE I. Lattice parameters, $\Delta\alpha$, and relative energies of ultrathin freestanding SnTe films. Experimentally, $\Delta\alpha(4\text{ AL}) > \Delta\alpha(2\text{ AL})$ [67]. The values reported for 2, 4 $AB + s$, 6, and 8 ALs correspond to ground-state structures.

Structure	a_1 (Å)	a_2 (Å)	$\Delta\alpha$, theory (deg)	$\Delta\alpha$, experiment (deg)	Energy difference (eV)
2 AL	4.728	4.567	2.02	1.4 ± 0.1	
4 AL, *AA*	4.668	4.566	1.28		0.0145
4 AL, *AB*	4.662	4.565	1.22		0.0150
4 AL, $AB + s$	4.766	4.565	2.52	1.9 ± 0.1	0.0000
6 AL, *AAA*	4.656	4.563	1.18		
8 AL, *AAAA*	4.651	4.564	1.09		

can be seen surrounded by an asymmetric density in the simulated image, with a larger (smaller) density above (below) the zero-density spot. In addition, the overall size of the simulated feature matches the size of the vacancy-related state observed in our experiments. The direction of the electric dipole **P** matches the experimental polarization too [68].

The simulated STM image originating from a Te vacancy in Fig. 3(d) has features inconsistent with the experimental STM displayed in Fig. 3(c) at an energy and isodensity identical to those used in Fig. 3(c), implying that the experimentally observed feature is not a Te vacancy. In turn, Fig. 3(e) is the simulated STM image obtained after removal of a Sn atom from the upper sublayer and a Te atom from the lower sublayer. There, the bright-dark contrast is not as extended as in the case of the single Sn vacancy. In summary, the comparison between experiment and simulations allows us to affirm that the vacancies are due to Sn atoms, which dope these SnTe films with holes.

C. Antiferroelectrically coupled 4-AL SnTe films

The ferroelectric coupling exemplified in Figs. 4(a) and 4(b) has importance for electrostatic energy storage applications because antiferroelectrically coupled ferroelectrics, such as the structure in Fig. 4(b), have been argued to lead to ultrahigh-density capacitors.

Up to now, antiferroelectric coupling has been induced by substitutional doping [86], making it relevant to know whether 4-AL SnTe realizes a ferroelectric coupling where consecutive pairs of 2 ALs have a parallel orientation of their in-plane polarization **P** [see Fig. 4(a)], or an antiferroelectric behavior in which consecutive 2 ALs have antiparallel in-plane polarizations [see Fig. 4(b)].

Three complementary experimental features have been employed to determine the ferroelectric coupling of the 4-AL SnTe film [67]: (i) the height profile, (ii) the band bending at the exposed ends, and (iii) the magnitude of $\Delta\alpha$ from the Fourier transform of the STM image. Band bending is larger on a ferroelectrically coupled (*AA*) 4-AL SnTe film when compared to an antiferroelectrically coupled (*AB*) 4-AL SnTe film because the electric field lines cancel out at the exposed edge in the latter case [67,68].

Here, we use energetics and the experimental values of $\Delta\alpha$ for 2 and 4 ALs to demonstrate an antiferroelectric coupling on 4-AL SnTe that is at odds with previous claims of ferroelectric coupling [65,71] and consistent with experiment [67,68].

In the present calculations, the *AA* structure shown in Fig. 4(a) has two 2 ALs relatively displaced along the z direction. The structure shown in Fig. 4(b) and labeled $AB + s$ (short for $AB+$ shift) has the following coordinates:

$$\mathbf{b}_1 = (a_1/2 + \delta_2, a_2/2, z_1)\ \text{Sn},$$
$$\mathbf{b}_2 = (\delta_1, 0.0, 0.0)\ \text{Sn},$$
$$\mathbf{b}_3 = (0.0, 0.0, z_3)\ \text{Te},$$

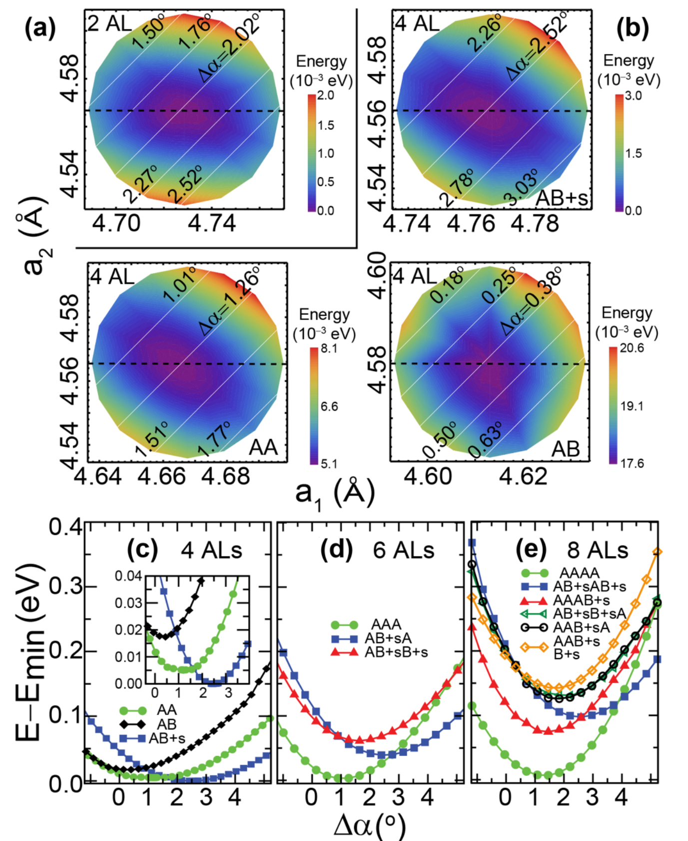

FIG. 5. Relative energy as a function of a_1 and a_2 for (a) 2-AL SnTe and (b) 4-AL SnTe in the $AB + s$, *AA*, and *AB* configurations. Diagonal lines in solid white in (a) and (b) denote a constant value of $\Delta\alpha$. (c) The trends were drawn over constant a_2 lines that cross the minimum energy point, shown as dashed lines in (b). (d) and (e): Energy for 6 and 8 ALs drawn over constant a_2 lines, respectively, that include their absolute minimum energies. Every 2 ALs on the 4-AL film are antiferroelectrically coupled, while successive 2-AL layers in thicker films are ferroelectrically coupled.

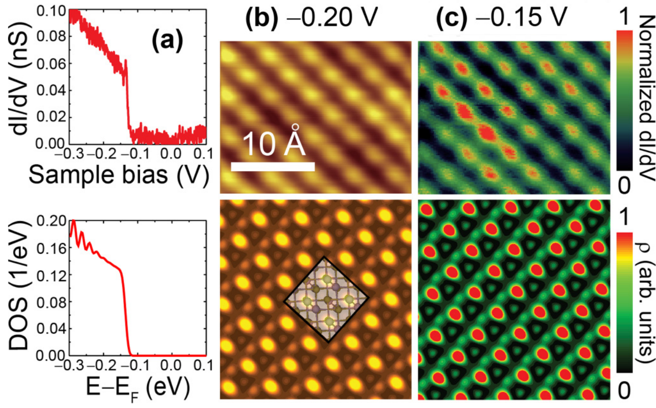

FIG. 6. (a) dI/dV spectra and DOS for a 4-AL SnTe film. The simulated structure has an $AB + s$ (antiferroelectric) interlayer coupling. (b) Experimental (top) and simulated (bottom) STM images at a bias voltage of -0.2 V. (c) Top: scanning tunneling spectroscopy images at $V_s = -0.15$ V, with a set point current $I_t = 100$ pA and a sample bias modulation $V_{\text{mod}} = 0.001$ V. Bottom: electronic density integrated in between -0.16 and -0.14 eV.

$$\mathbf{b}_4 = (a_1/2, a_2/2, z_1 - z_3) \text{ Te},$$
$$\mathbf{b}_5 = (a_1 - \delta_1, a_2/2, z_1 + \Delta) \text{ Sn},$$
$$\mathbf{b}_6 = (a_1/2 - \delta_2, 0.0, \Delta) \text{ Sn},$$
$$\mathbf{b}_7 = (a_1/2, 0.0, z_3 + \Delta) \text{ Te},$$
$$\mathbf{b}_8 = (a_1, a_2/2, z_1 - z_3 + \Delta) \text{ Te},$$

with $\delta_1 = 0.316$, $\delta_2 = 0.307$, $z_1 = 3.182$, $z_3 = 2.967$, and $\Delta = 6.179$ (all in Å) and a_1, a_2 provided in Table I.

The structures shown in Figs. 1 and 4 are the result of a full structural optimization using a dense meshing procedure in which a_1 and a_2 are preset to fine-mesh locations, and only atomic positions are relaxed. This procedure yields the energy versus a_1, a_2 plots shown in Fig. 5(a), in which iso-$\Delta\alpha$ lines resulting from Eq. (1) are displayed as well. The optimal lattice constants and relative energies are reported in Table I for each of these structures too. Labels *AA*, *AAA*, and *AAAA* on this Table stand for ferroelectric coupling among layers.

Figure 5(c) provides one-dimensional plots cutting across $\Delta\alpha$ paths that capture the absolute minima in Fig. 5(b), to compare energetics versus the relative placement of consecutive 2 ALs. The most important point from Fig. 5 is that the lowest-energy 4-AL structure is antiferroelectrically coupled.

Figure 6 displays experimental (top row) and computational (bottom row) results supporting the antiferroelectric coupling of a 4 AL SnTe slab [68]. There, the empirical relation $dI/dV \simeq 0.5 \times$ DOS [established in Fig. 2(a)] can be seen again. Furthermore, the locations of bright spots between experimental and simulated STM images agree in Figs. 6(b) and 6(c) and the elongation of the bright spot continues to indicate the orientation of the dipole moment on the scanned surface, to the point that such observed elongation feature can be added to conditions (i)–(iii) expressed earlier on. Despite the increased spatial resolution of the simulated STM image integrated in between -0.16 and -0.14 eV when compared with its experimental counterpart [Fig. 6(c)], the dark diagonal feature can be observed along the elongated direction (a_1) in both images. Following Eq. (1), such relative elongation of a_1 with respect to a_2 that leads to the asymmetric dark diagonal lines at -45° is necessary to achieve the experimental value of $\Delta\alpha$.

In conclusion, experiment [67,68] and the present calculations confirm an antiferroelectric coupling of 4 AL SnTe films, while Table I and Fig. 5 indicate that unsupported films with more than 4 ALs are ferroelectrically coupled.

D. Atomistic structure and electronic band structures of thicker films

The antiferroelectric coupling of 4-AL SnTe and the ferroelectric coupling on the rhombic bulk discussed thus far imply the existence of a critical thickness at which the antiferroelectrically coupled thin films transition onto a (bulklike) ferroelectrically coupled SnTe.

Previous observation invites us to examine the ferroelectric coupling of thicker films following the bottom-up approach

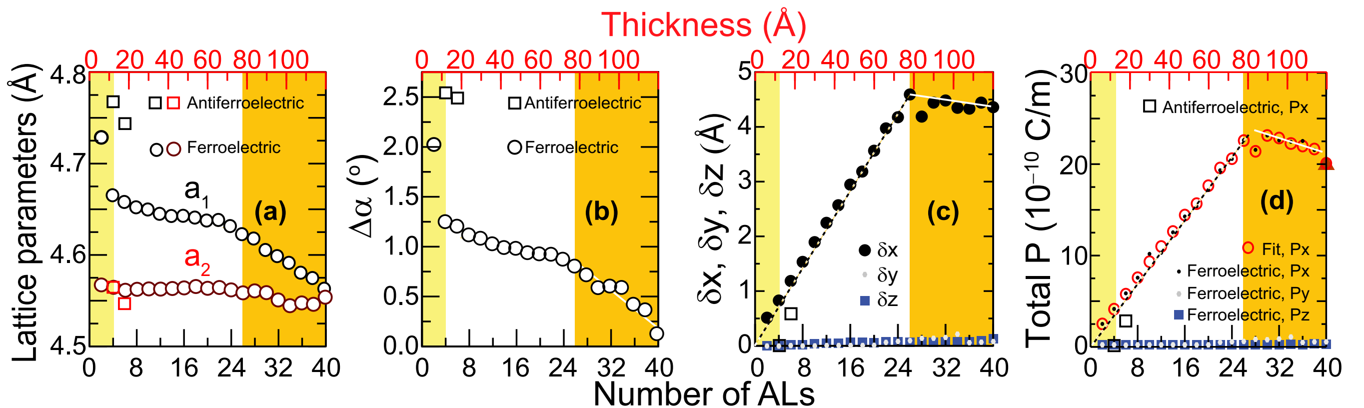

FIG. 7. Thickness dependence of (a) in-plane lattice parameters a_1 and a_2, (b) rhombic distortion angle $\Delta\alpha$, (c) structural distortions (δ_x, δ_y, δ_z), and (d) total electric dipole $\mathbf{P}$ for SnTe films from 2 to 40 ALs. Circles correspond to a ferroelectric (*AA*) coupling among consecutive 2 ALs, while open squares describe slabs with an antiferroelectric coupling. Yellow, white, and orange boxes were drawn to emphasize three specific trend regions.

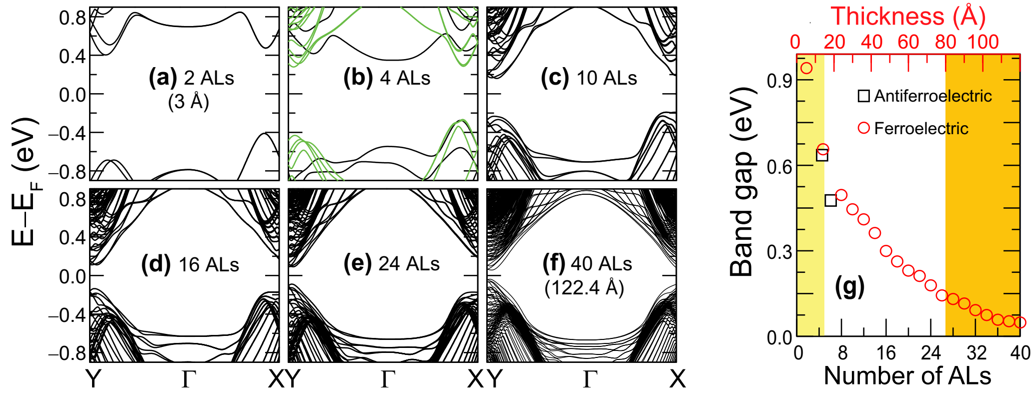

FIG. 8. Thickness dependence of the electronic band structure of SnTe films of selected thicknesses: (a) 2 ALs, (b) 4 ALs (green bands correspond to the $AB + s$ phase, and black bands correspond to the AA phase), (c) 10 ALs, (d) 16 ALs, (e) 24 ALs, and (f) 40 ALs. These band structure plots were obtained with the spin-orbit coupling turned on. (g) The magnitude of the electronic band gap decreases as the number of ALs is increased, but it does not become zero due to the non-rocksalt nature of these slabs (i.e., due to their lower symmetry).

pursued thus far. To this end, and as reported in Figs. 5(d) and 5(e), 6 AL and 8 AL SnTe slabs were first considered, showing that ferroelectric coupling is preferred in both instances. For that reason, all thicker films were stacked in a ferroelectric fashion consistent with bulk SnTe. Reference [69] indicates that films with a thickness in excess of 100 Å, corresponding to about 36 ALs, behave as bulk SnTe. Using such experimental guidance to set an upper thickness limit, the dependencies of in-plane lattice parameters a_1 and a_2 and $\Delta\alpha$ on thickness for SnTe films ranging from 2 to 40 ALs as obtained computationally are shown in Figs. 7(a) and 7(b), respectively. Data shown by circles in Fig. 7 corresponds to a ferroelectric coupling among consecutive 2 ALs, while squares at the left ends of these plots describe slabs with antiferroelectric coupling. The similar trends between a_1 and $\Delta\alpha$ in Figs. 7(a) and 7(b) arise from the linear dependency of $\Delta\alpha$ on a_1/a_2 in Eq. (1) and the almost constancy of a_2 in Fig. 7(a).

There is an abrupt increase in a_1 and $\Delta\alpha$ in going from 2 to 4 ALs, as the antiferroelectrically-stacked structure increases a_1 [squares in Figs. 7(a)] at the expense of reducing its dipole moment down to zero in Fig. 7(d). The area in white in Fig. 7(a) shows an almost constant a_2 and a decay of a_1 by 0.0013 Å per AL, making $\Delta\alpha$ in Fig. 7(b) decay by 0.025° per AL as the SnTe film gradually turns into a bulk structure. Between 30 and 40 ALs, the decay of a_1 and $\Delta\alpha$ in Figs. 7(a) and 7(b) becomes more drastic (0.0042 Å and 0.050° per AL, respectively), so that $\Delta\alpha \sim 0.1°$ at 40 ALs in Fig. 7(b).

Atomistic displacements δ_x, δ_y, and δ_z among anion and cations on a given 2 ALs shown in Fig. 1 can be linked to the total polarization observed in these slabs. In order to characterize atomistic displacements for thicker slabs, we define:

$$\delta x \equiv \sum_{n=1}^{N/2} \sum_{i=1}^{2} \delta x_{i,n} \tag{2}$$

as the sum of displacements along the x direction for a given layer as indicated in Fig. 1(c), where N is the number of ALs in a given slab (there are two displacements per 2 ALs), with similar expressions for δy and δz. These sums of displacements are displayed in Fig. 7(c). There, δx increases by 0.17 Å per AL up to 26 ALs and then slightly decreases for thicknesses between 28 and 40 ALs as a result of the sudden compression of a_1 seen in Fig. 7(a). In turn, δy and δz remain equal to zero.

In Fig. 7(d), the electric dipole $\mathbf{P}$ of a 2 AL slab was computed using the standard Berry phase approach [87] and linked it to the magnitude of δx. (We computed $\mathbf{P}$ using the VASP code [88,89] on the structures discussed thus far, that were obtained with the SIESTA code.) This permitted adding the electric dipole's modulus on the standard Berry phase estimation to a periodic term that was consistent with the magnitude of δx. The total polarization increases by 0.9×10^{-10} C/m per AL up to 26 ALs. From then on, both δ_x and P_x decrease at a rate of 0.02 Å per AL and 0.4×10^{-10} C/m per AL up to 40 ALs. The sudden drop in a_1 past 30 ALs does reduce the overall magnitude of δx despite the subsequent addition of monolayers, but it never brings the dipole all the way to zero for what would be a rocksalt conformation. Instead, the reported nonzero dipole is linked to the rhombic nature of films containing more than 4 ALs.

Last, we display the electronic structure with spin-orbit coupling turned on for SnTe slabs with increasing thicknesses in Figs. 8(a)–8(f). Figure 8(a) displays the 2 AL SnTe slab as an indirect band gap semiconductor [90]. As seen in Fig. 8(b), such an indirect band gap remains for 4-AL SnTe with *AA* (black lines) and antiferroelectric stacking (green lines) and up to 8 ALs.

Even though the band structure is not symmetric around the X and Y points in Fig. 8(c), the band gap becomes direct for a thickness of 10 ALs. Seeing the full sequence of subplots, Figs. 8(a)–8(f), the band gap decreases in value as the thickness increases but it never closes in Fig. 8(g) as the slab never turns onto a rocksalt structure, which means that metallic surface states [54] do not develop [56].

IV. CONCLUSION

Despite of its longevity, SnTe remains an important material in condensed-matter physics, and the structural

evolution of SnTe from 2 to 40 ALs has been provided here. Four-AL SnTe favors an antiferroelectric coupling, while suspended films with thicknesses ranging from 6 to 40 ALs were ferroelectrically coupled. The evolution of the rhombic distortion angle, the electric polarization, and the electronic band structure have been provided as well. The atomistic structures and resulting electric dipole moments and electronic band structures were found to be different from those obtained by capping bulk structures, especially for ultrathin films. The information provided here is expected to help us better understand the coupling among atomistic structures and the fascinating material properties of SnTe slabs.

ACKNOWLEDGMENTS

Research at Arkansas was supported by the U.S. Department of Energy, Office of Basic Energy Sciences, Division of Materials Science and Engineering, under Early Career Award No. DE-SC0016139. Calculations were performed at the Center for Nanoscale Materials at Argonne National Laboratory (CNM User Proposal 57959). K.C. and S.S.P.P. were funded by the Deutsche Forschungsgemeinschaft (DFG, German Research Foundation), Project No. PA 1812/2-1. K.C., Q.-K.X., X.C., and S.-H.J. were supported by the National Natural Science Foundation of China (Grant No. 51561145005) and Ministry of Science and Technology of China (Grant No. 2016YFA0301002).

[1] P. B. Littlewood, J. Phys. C **13**, 4855 (1980).
[2] C. Kittel, *Introduction to Solid State Physics* (Wiley, New York, 1953), Chap. 1, p. 14.
[3] G. Tan, L.-D. Zhao, F. Shi, J. W. Doak, S.-H. Lo, H. Sun, C. Wolverton, V. P. Dravid, C. Uher, and M. G. Kanatzidis, J. Am. Chem. Soc. **136**, 7006 (2014).
[4] L.-D. Zhao, S.-H. Lo, Y. Zhang, H. Sun, G. Tan, C. Uher, C. Wolverton, V. P. Dravid, and M. G. Kanatzidis, Nature (London) **508**, 373 (2014).
[5] E. E. Vago and R. F. Barrow, Proc. Phys. Soc. **58**, 707 (1946).
[6] R. Brebrick, J. Phys. Chem. Solids **24**, 27 (1963).
[7] D. H. Damon, C. R. Martin, and R. C. Miller, J. Appl. Phys. **34**, 3083 (1963).
[8] J. N. Zemel, J. D. Jensen, and R. B. Schoolar, Phys. Rev. **140**, A330 (1965).
[9] H. Riedl, R. Schoolar, and B. Houston, Solid State Commun. **4**, 399 (1966).
[10] J. R. Burke, R. S. Allgaier, B. B. Houston, J. Babiskin, and P. G. Siebenmann, Phys. Rev. Lett. **14**, 360 (1965).
[11] H. T. Savage, B. Houston, and J. R. Burke, Phys. Rev. B **6**, 2292 (1972).
[12] R. S. Allgaier and B. Houston, Phys. Rev. B **5**, 2186 (1972).
[13] A. K. Okazaki, S. Wiedmann, S. Pezzini, M. L. Peres, P. H. O. Rappl, and E. Abramof, Phys. Rev. B **98**, 195136 (2018).
[14] J. R. Burke and H. R. Riedl, Phys. Rev. **184**, 830 (1969).
[15] P. Lin, W. Saslow, and M. L. Cohen, Solid State Commun. **5**, 893 (1967).
[16] L. M. Rogers, J. Phys. D **1**, 845 (1968).
[17] Y. W. Tung and M. L. Cohen, Phys. Rev. **180**, 823 (1969).
[18] K. M. Rabe and J. D. Joannopoulos, Phys. Rev. B **32**, 2302 (1985).
[19] R. Tsu, W. E. Howard, and L. Esaki, Phys. Rev. **172**, 779 (1968).
[20] P. C. Kemeny and M. Cardona, J. Phys. C **9**, 1361 (1976).
[21] P. B. Littlewood, B. Mihaila, R. K. Schulze, D. J. Safarik, J. E. Gubernatis, A. Bostwick, E. Rotenberg, C. P. Opeil, T. Durakiewicz, J. L. Smith, and J. C. Lashley, Phys. Rev. Lett. **105**, 086404 (2010).
[22] K. L. I. Kobayashi, Y. Kato, Y. Katayama, and K. F. Komatsubara, Phys. Rev. Lett. **37**, 772 (1976).
[23] A. D. C. Grassie, J. A. Agapito, and P. Gonzalez, J. Phys. C **12**, L925 (1979).
[24] S. Katayama and D. L. Mills, Phys. Rev. B **22**, 336 (1980).
[25] P. B. Allen and M. L. Cohen, Phys. Rev. **177**, 704 (1969).
[26] R. A. Hein and P. H. E. Meijer, Phys. Rev. **179**, 497 (1969).
[27] W. Keune, Phys. Rev. B **10**, 5057 (1974).
[28] L. J. Brillson, E. Burstein, and L. Muldawer, Phys. Rev. B **9**, 1547 (1974).
[29] T. Shimada, K. L. I. Kobayashi, Y. Katayama, and K. F. Komatsubara, Phys. Rev. Lett. **39**, 143 (1977).
[30] G. S. Pawley, W. Cochran, R. A. Cowley, and G. Dolling, Phys. Rev. Lett. **17**, 753 (1966).
[31] J. F. Scott, Rev. Mod. Phys. **46**, 83 (1974).
[32] M. Iizumi, Y. Hamaguchi, K. F. Komatsubara, and Y. Kato, J. Phys. Soc. Jpn. **38**, 443 (1975).
[33] A. J. Bevolo, H. R. Shanks, and D. E. Eckels, Phys. Rev. B **13**, 3523 (1976).
[34] K. R. Knox, E. S. Bozin, C. D. Malliakas, M. G. Kanatzidis, and S. J. L. Billinge, Phys. Rev. B **89**, 014102 (2014).
[35] C. W. Li, O. Hellman, J. Ma, A. F. May, H. B. Cao, X. Chen, A. D. Christianson, G. Ehlers, D. J. Singh, B. C. Sales, and O. Delaire, Phys. Rev. Lett. **112**, 175501 (2014).
[36] R. B. Shalvoy, G. B. Fisher, and P. J. Stiles, Phys. Rev. B **15**, 1680 (1977).
[37] C. D. O'Neill, D. A. Sokolov, A. Hermann, A. Bossak, C. Stock, and A. D. Huxley, Phys. Rev. B **95**, 144101 (2017).
[38] E. R. Cowley, J. K. Darby, and G. S. Pawley, J. Phys. C **2**, 1916 (1969).
[39] A. Natori, J. Phys. Soc. Jpn. **41**, 782 (1976).
[40] P. B. Littlewood, J. Phys. C **13**, 4875 (1980).
[41] H. Bilz, H. Büttner, A. Bussmann-Holder, W. Kress, and U. Schröder, Phys. Rev. Lett. **48**, 264 (1982).
[42] D. Strauch and R. Becher, J. Phys. C **20**, 1641 (1987).
[43] E. Cowley, Physica A (Amsterdam, Neth.) **232**, 585 (1996).
[44] N. S. Gillis, Phys. Rev. Lett. **22**, 1251 (1969).
[45] N. S. Gillis and T. R. Koehler, Phys. Rev. B **5**, 1925 (1972).
[46] A. G. Beattie, J. Appl. Phys. **40**, 4818 (1969).
[47] D. H. Damon, J. Appl. Phys. **37**, 3181 (1966).
[48] C. W. Li, J. Ma, H. B. Cao, A. F. May, D. L. Abernathy, G. Ehlers, C. Hoffmann, X. Wang, T. Hong, A. Huq, O. Gourdon, and O. Delaire, Phys. Rev. B **90**, 214303 (2014).
[49] O. Madelung, U. Rössler, and M. Schulz (eds.), Tin telluride (SnTe) crystal structure, lattice parameters, in *Non-tetrahedrally Bonded Elements and Binary Compounds I* (Springer, Berlin, 1998), pp. 1–8.

[50] S. Sugai, K. Murase, and H. Kawamura, Solid State Commun. **23**, 127 (1977).
[51] W. Jantsch, Dielectric properties and soft modes in semiconducting (Pb, Sn, Ge)Te, in *Dynamical Properties of IV-VI Compounds* (Springer, Berlin, 1983), pp. 1–50.
[52] E. Fradkin, E. Dagotto, and D. Boyanovsky, Phys. Rev. Lett. **57**, 2967 (1986).
[53] O. Pankratov, Phys. Lett. A **121**, 360 (1987).
[54] T. H. Hsieh, H. Lin, J. Liu, W. Duan, A. Bansil, and L. Fu, Nat. Commun. **3**, 982 (2012).
[55] Y. Tanaka, Z. Ren, T. Sato, K. Nakayama, S. Souma, T. Takahashi, K. Segawa, and Y. Ando, Nat. Phys. **8**, 800 (2012).
[56] E. Plekhanov, P. Barone, D. Di Sante, and S. Picozzi, Phys. Rev. B **90**, 161108(R) (2014).
[57] X. Li, F. Zhang, Q. Niu, and J. Feng, Sci. Rep. **4**, 6397 (2014).
[58] B. Z. Rameshti and R. Asgari, Phys. Rev. B **94**, 205401 (2016).
[59] F. Schindler, A. M. Cook, M. G. Vergniory, Z. Wang, S. S. P. Parkin, B. A. Bernevig, and T. Neupert, Sci. Adv. **4**, eaat0346 (2018).
[60] A. K. Singh and R. G. Hennig, Appl. Phys. Lett. **105**, 042103 (2014).
[61] M. Mehboudi, A. M. Dorio, W. Zhu, A. van der Zande, H. O. H. Churchill, A. A. Pacheco-Sanjuan, E. O. Harriss, P. Kumar, and S. Barraza-Lopez, Nano Lett. **16**, 1704 (2016).
[62] L. Huang, F. Wu, and J. Li, J. Chem. Phys. **144**, 114708 (2016).
[63] C. Kamal, A. Chakrabarti, and M. Ezawa, Phys. Rev. B **93**, 125428 (2016).
[64] M. Wu, S.-H. Wei, and L. Huang, Phys. Rev. B **96**, 205411 (2017).
[65] K. Liu, J. Lu, S. Picozzi, L. Bellaiche, and H. Xiang, Phys. Rev. Lett. **121**, 027601 (2018).
[66] J. Slawinska, F. T. Cerasoli, H. Wang, S. Postorino, A. Supka, S. Curtarolo, M. Fornari, and M. B. Nardelli, 2D Mater. **6**, 025012 (2019).
[67] K. Chang, J. Liu, H. Lin, N. Wang, K. Zhao, A. Zhang, F. Jin, Y. Zhong, X. Hu, W. Duan, Q. Zhang, L. Fu, Q.-K. Xue, X. Chen, and S.-H. Ji, Science **353**, 274 (2016).
[68] K. Chang, T. P. Kaloni, H. Lin, A. Bedoya-Pinto, A. K. Pandeya, I. Kostanovskiy, K. Zhao, Y. Zhong, X. Hu, Q.-K. Xue, X. Chen, S.-H. Ji, S. Barraza-Lopez, and S. S. P. Parkin, Adv. Mater. **31**, 1804428 (2019).
[69] D. Zhang, H. Baek, J. Ha, T. Zhang, J. Wyrick, A. V. Davydov, Y. Kuk, and J. A. Stroscio, Phys. Rev. B **89**, 245445 (2014).
[70] K. Chang and S. S. P. Parkin, APL Mater. **7**, 041102 (2019).
[71] W. Wan, C. Liu, W. Xiao, and Y. Yao, Appl. Phys. Lett. **111**, 132904 (2017).
[72] J. M. Soler, E. Artacho, J. D. Gale, A. García, J. Junquera, P. Ordejón, and D. Sánchez-Portal, J. Phys.: Condens. Matter **14**, 2745 (2002).
[73] J. Junquera, O. Paz, D. Sánchez-Portal, and E. Artacho, Phys. Rev. B **64**, 235111 (2001).
[74] N. Troullier and J. L. Martins, Phys. Rev. B **43**, 1993 (1991).
[75] P. Hyldgaard, K. Berland, and E. Schröder, Phys. Rev. B **90**, 075148 (2014).
[76] G. Román-Pérez and J. M. Soler, Phys. Rev. Lett. **103**, 096102 (2009).
[77] P. Rivero, V. M. García-Suárez, D. Pereñiguez, K. Utt, Y. Yang, L. Bellaiche, K. Park, J. Ferrer, and S. Barraza-Lopez, Comput. Mater. Sci. **98**, 372 (2015).
[78] H. J. Monkhorst and J. D. Pack, Phys. Rev. B **13**, 5188 (1976).
[79] J. Tersoff and D. R. Hamann, Phys. Rev. Lett. **50**, 1998 (1983).
[80] D. Tománek and S. G. Louie, Phys. Rev. B **37**, 8327 (1988).
[81] K. T. He, J. C. Koepke, S. Barraza-Lopez, and J. W. Lyding, Nano Lett. **10**, 3446 (2010).
[82] J. C. Koepke, J. D. Wood, C. M. Horvath, J. W. Lyding, and S. Barraza-Lopez, Appl. Phys. Lett. **107**, 071603 (2015).
[83] P. Rivero, C. M. Horvath, Z. Zhu, J. Guan, D. Tománek, and S. Barraza-Lopez, Phys. Rev. B **91**, 115413 (2015).
[84] J. Hass, F. Varchon, J. E. Millán-Otoya, M. Sprinkle, N. Sharma, W. A. de Heer, C. Berger, P. N. First, L. Magaud, and E. H. Conrad, Phys. Rev. Lett. **100**, 125504 (2008).
[85] S. Barraza-Lopez, T. P. Kaloni, S. P. Poudel, and P. Kumar, Phys. Rev. B **97**, 024110 (2018).
[86] B. Xu, J. Íñiguez, and L. Bellaiche, Nat. Commun. **8**, 15682 (2017).
[87] R. Resta and D. Vanderbilt, *Physics of Ferroelectrics* (Springer, Berlin, 2007), pp. 31–68.
[88] G. Kresse and J. Furthmüller, Phys. Rev. B **54**, 11169 (1996).
[89] G. Kresse and D. Joubert, Phys. Rev. B **59**, 1758 (1999).
[90] L. C. Gomes and A. Carvalho, Phys. Rev. B **92**, 085406 (2015).